The Astrophysical Journal, 927:43 (13pp), 2022 March 1 https://doi.org/10.3847/1538-4357/ac4588

High-latitude Observations of Inertial-range Turbulence by the Ulysses Spacecraft During the Solar Minimum of 1993–96

Abigale S. Watson[1,2], Charles W. Smith[1], Anastasia V. Marchuk[1], Matthew R. Argall[1], Colin J. Joyce[1], Philip A. Isenberg[1], Bernard J. Vasquez[1], Nathan A. Schwadron[1], Maciej Bzowski[3], Marzena A. Kubiak[3], and Neil Murphy[4]

[1] Physics Department and Space Science Center, Morse Hall, University of New Hampshire, Durham, NH 03824, USA; abbey@tage.com, Charles.Smith@unh.edu, Anastasia.V.Marchuk@gmail.com, Matthew.Argall@unh.edu, Colin.Joyce@unh.edu, Phil.Isenberg@unh.edu, Bernie.Vasquez@unh.edu, Nathan.Schwadron@unh.edu

[2] Department of Mechanical Engineering, Wentworth Institute of Technology, Boston, MA 02115, USA

[3] Space Research Centre, Polish Academy of Sciences, (CBK PAN), Warsaw, Bartycka 18A, Poland; Bzowski@cbk.waw.pl, MKubiak@cbk.waw.pl

[4] Jet Propulsion Laboratory, Mail Stop 180-600, 4800 Oak Grove Drive, Pasadena, CA 91109, USA; Neil.Murphy@jpl.nasa.gov

Received 2021 October 7; revised 2021 November 9; accepted 2021 November 22; published 2022 March 3

Abstract

We have examined Ulysses magnetic field measurements for the years 1993 through 1996 as the spacecraft moved sunward from 5 au at high southern latitudes, passing through perihelion during the first fast-latitude scan to achieve high northern latitudes, and finally returning to 5 au. These years represent near-solar-minimum activity, providing a clear measure of high-latitude solar-wind turbulence. We apply a series of tests to the data, examining both the magnetic variance anisotropy and the underlying wavevector anisotropy, finding them to be consistent with past 1 au observations. The variance anisotropy depends upon both the thermal proton temperature parameter and the amplitude of the magnetic power spectrum, while the underlying wavevector anisotropy is dominated by the component perpendicular to the mean magnetic field. We also examine the amplitude of the magnetic power spectrum as well as the associated turbulent transport of energy to small scales that results in the heating of the thermal plasma. The measured turbulence is found to be stronger than that seen at low latitudes by the Voyager spacecraft as it traverses the distance from 1 to 5 au during the years approaching solar maximum. If the high- and low-latitude sources are comparable, this would indicate that while the heating processes are active in both regions, the turbulence has had less decay time in the transport of energy to small scales. Alternatively, it may also be that the high-latitude source is stronger.

Unified Astronomy Thesaurus concepts: Solar wind (1534); Interplanetary turbulence (830); Interplanetary magnetic fields (824); Magnetohydrodynamics (1964); Space plasmas (1544)

1. Introduction

It has become increasingly well established that the repeatable features of solar-wind fluctuations, including the magnetic, velocity, and density spectra, are evidence that solar-wind fluctuations are dominated by the nonlinear dynamics of magnetohydrodynamics (MHD). This does not preclude the natural variability as a result of solar activity or solar-wind conditions. The turbulent dynamics result in the significant in situ heating of the plasma. Most of the effort to develop observational standards to characterize the turbulence has been developed using observations at 1 au. These efforts have left open questions about the nature of turbulence at high latitudes, especially during solar-minimum conditions, when strong cross-field correlations—often called imbalanced turbulence—may weaken the nonlinear dynamics.

Diverse theories based upon divergent views of the nonlinear MHD dynamics have lead to differing opinions regarding the fundamental nature of the solar-wind fluctuations. One view holds that MHD can be described as the magnetic extension of traditional hydrodynamics (Kolmogorov 1941; Matthaeus & Zhou 1989; Leamon et al. 1999; Smith 2009; Matthaeus & Velli 2011). Another view holds that MHD turbulence is best described as interacting waves that are either solutions to the linear or nonlinear wave equations (Iroshnikov 1964; Kraichnan 1965; Howes et al. 2008a, 2008b, 2008c; Smith et al. 2012). Despite the divergence of views, there are observational tests that can be used to characterize the turbulent dynamics in such a way that any theory must meet the observations.

In a companion paper (Marchuk et al. 2021), we use many of the same techniques as are employed in this paper to study Ulysses observations of waves excited by newborn interstellar He^+. Here, we select four years of Ulysses data spanning the first fast-latitude scan at solar minimum and incorporating the years from the first Jupiter flyby at ~5 au, to periapsis, and back to 5 au. The majority of observations reported here are recorded at high latitudes during solar minimum. There are no events used here that show evidence of wave excitation by suprathermal particles. Since waves due to interstellar pickup ions exist during times when the turbulent energy transport rate is weaker than the wave-excitation rate (Cannon et al. 2014b; Aggarwal et al. 2016; Fisher et al. 2016; Hollick et al. 2018b), this might suggest that we have biased the database by excluding weak-turbulence intervals. In reality, there are only two instances of waves due to pickup H^+ inside 4 au during this time and no instances of waves due to He^+. The remaining examples found during the four years studied here exist beyond 4 au at heliolatitudes below 35°. Therefore, we do not believe that we have biased this analysis.

In Section 2 we review the methods of analysis used in this paper. Section 3 provides an overview of the solar-wind

conditions that form the database for this analysis. In Section 4 we present the fluctuation anisotropy as described by Belcher & Davis (1971) for low-latitude 1 au observations and find that they depend equally upon the proton thermal parameter and turbulent amplitude as seen at 1 au (Smith et al. 2006c). The unrelated wavevector anisotropy as computed from the fluctuation anisotropy of the two magnetic components perpendicular to the mean magnetic field (Bieber et al. 1996) is computed in Section 5 and found to closely resemble 1 au results for both high- and low-speed winds at 1 au (Hamilton et al. 2008). The exception to this is magnetic clouds seen at 1 au, which are observed to have a much larger fraction of field-aligned wavevectors. The analysis of the turbulent energy cascade and resulting solar-wind heating is performed in Section 6, where we find that the high-latitude solar-minimum turbulence level exceeds what is reported at low latitudes during the rise to solar maximum.

2. Data Analysis Methods

The work presented here is part of a larger effort to study solar-wind turbulence and the excitation of low-frequency waves by newborn interstellar pickup ions, most notably H^+ and He^+. These waves are excited at spacecraft-frame frequencies $f_{sc} > f_{ic}$, where f_{sc} denotes fluctuation frequencies as measured in the spacecraft frame and $f_{ic} = e_i B/(2\pi m_i c)$ (where e_i is the charge of the ion, B is the mean magnetic field strength, m_i is the ion mass, and c is the speed of light) is the cyclotron frequency of the ion in question. Waves observed by the Ulysses spacecraft due to pickup H^+ were analyzed and discussed by Cannon et al. (2013, 2014a, 2014b, 2017), and waves excited by pickup He^+ were analyzed and discussed by Marchuk et al. (2021). While we employ the same techniques used in those papers to identify and analyze intervals of interest, here we introduce alternate questions and techniques to better characterize the nonlinear dynamics that are responsible for the formation of the turbulent spectrum.

This investigation will include the polarization analyses we normally employ in related studies of waves due to newborn interstellar pickup ions (Joyce et al. 2010; Cannon et al. 2014a, 2014b; Argall et al. 2015, 2017, 2018; Aggarwal et al. 2016; Fisher et al. 2016; Smith et al. 2017; Hollick et al. 2018a, 2018b, 2018c). We do this for two reasons. First, we will use the polarization spectra to identify and exclude data intervals that contain waves attributable to newborn pickup ions. Second, we will characterize intervals of solar-wind turbulence that are without evidence of wave excitation by suprathermal particle populations.

Polarization analyses are performed using the fast Fourier transform (FFT) technique, where FFTs of time series are computed and polarization parameters are computed from the Fourier transforms (Fowler et al. 1967; Rankin & Kurtz 1970; Means 1972; Mish et al. 1982). These are the same analyses we have used in related studies (Smith et al. 1990; Leamon et al. 1998a, 1998b; Smith et al. 2006a, 2006c; Hamilton et al. 2008; Markovskii et al. 2008, 2015; Argall et al. 2015, 2017; Fisher et al. 2016; Hollick et al. 2018a; Pine et al. 2020b). The degree of polarization, D_{pol}, is the fraction of the polarized power in the total power spectrum as computed from the diagonal terms of the power spectral matrix. The coherence, C_{oh}, is computed from the off-diagonal terms in the power spectral matrix and offers a measure of the cross-component correlation of the fluctuations. The ellipticity, E_{lip}, is the ratio of the minimum-to-maximum variance axes of the fluctuation ellipse and carries the sign of the polarization, with $E_{lip} > 0$ ($E_{lip} < 0$) representing right-hand (left-hand) polarized fluctuations in the spacecraft frame. Also, $|E_{lip}| = 1$ ($E_{lip} = 0$) represents circular (linear) polarization. The minimum-variance direction represents the direction of propagation relative to the mean magnetic field, although this analysis is incapable of distinguishing between parallel and antiparallel propagation. The angle between the minimum-variance direction and the mean field, $\Theta_{kB} \equiv \arccos(\hat{\boldsymbol{k}} \cdot \hat{\boldsymbol{B}})$, is defined so that $0° \leqslant \Theta_{kB} \leqslant 90°$.

Computation of the power spectrum via the Blackman–Tukey method is performed via the Fourier transform of the autocorrelation function (Blackman & Tukey 1958; Matthaeus & Goldstein 1982). Fundamental concepts of hydrodynamic turbulence lead to the use of this definition naturally (Batchelor 1953). Prewhitening of the autocorrelation function using a first-order difference filter elevates the power in the higher frequencies and reduces spectral leakage, thereby better resolving changes in spectral slope. This must be corrected for by using a post-darkening filter after the spectrum is computed in order to return the computed spectrum to the true underlying form (Chen 1989). The analyses shown here build upon observations by the Advanced Composition Explorer (ACE), Voyager, and Wind spacecraft (Leamon et al. 1998a; Smith et al. 2006a, 2006b; Hamilton et al. 2008; Pine et al. 2020a, 2020b, 2020c, 2020d).

Figure 1 shows three examples of the type of solar-wind turbulence magnetic field spectra from the Ulysses Magnetometer (MAG) employed here. Each panel shows four spectra: the spectrum of each of the three components in mean-field coordinates and the trace of the power spectral density matrix. The red lines are best fits to the measured spectra over the frequencies shown (2–50 mHz) and excluding the range $0.8 f_{p,c} < f_{sc} < 2.2 f_{p,c}$ to avoid any contamination of the results from wave excitation by newborn interstellar pickup ions (Marchuk et al. 2021). In the top two panels, all of the fit spectra are statistically equivalent to $f^{-5/3}$ while the bottom panel shows spectra consistent with $f^{-1.58}$. This is well within the normal variability of results. Figure 1(top) shows an example with a clear spectral break at $f_{sc} \sim 0.07$ Hz marking the transition from the inertial range where energy-conserving spectral transport dominates the dynamics, to the dissipation range where collective fluctuations are converted into heat. At $f_{sc} > 0.2$ Hz high-frequency noise dominates the spectrum. It is unclear at this point whether the apparent noise exists at this frequency or is aliased from higher frequencies. Figure 1(middle) shows an example with a lower Nyquist frequency and without evidence of a dissipation range. The absence of a steepened spectrum does not mean that dissipation does not occur, and it may simply reflect the Nyquist frequency, but it is consistent with a reduced rate of dissipation (Smith et al. 2006a). Figure 1(bottom) shows an example with the onset of the dissipation spectrum at $f_{sc} \sim 0.15$ Hz. In this instance, there is only minimal aliasing at the highest frequencies.

3. Data Overview

Launched on 1990 October 6, the Ulysses spacecraft was initially sent to Jupiter at ∼5 au. Passing first over the Jovian north pole, and then under the south pole, placed the spacecraft in a sunward out-of-ecliptic orbit. The first fast-latitude scan occurred in early 1995 during solar minimum when the spacecraft reached a heliocentric distance of ∼1.3 au, the closest it would come to the Sun. The spacecraft continued in a

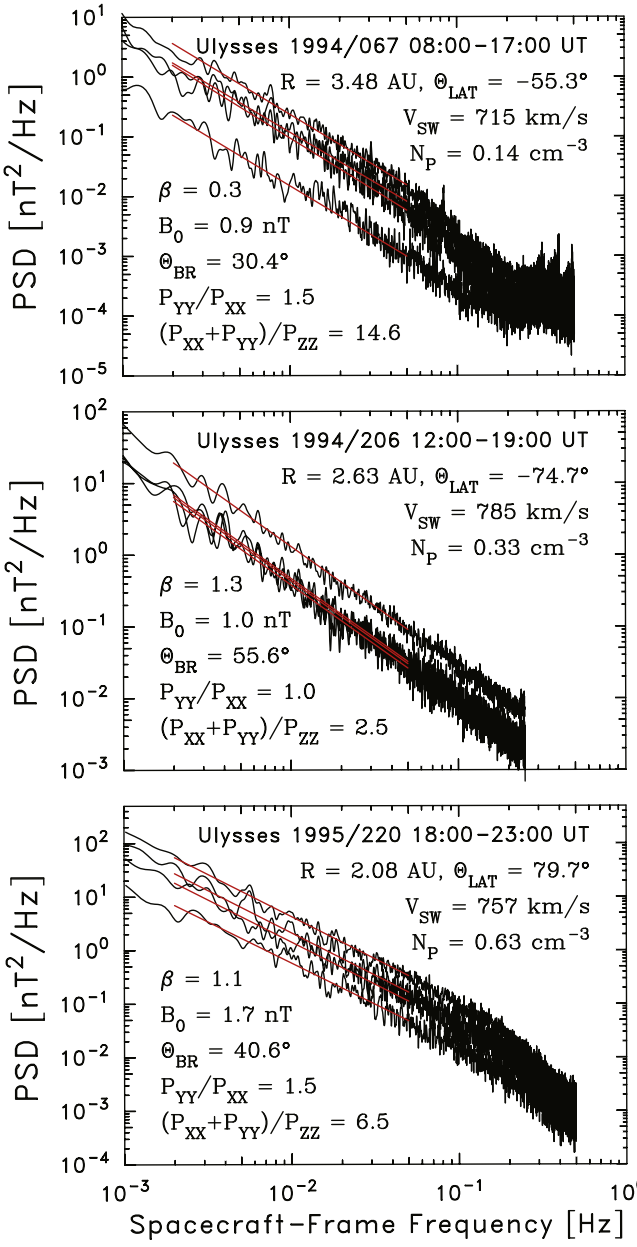

Figure 1. Three examples of the turbulent magnetic spectra measured by the Ulysses spacecraft from 1993 through 1996. See text for detailed descriptions.

high-latitude orbit from there, returning to where Jupiter had been formerly but had since moved, only to fall sunward again. Ulysses completed three fast-latitude scans and almost three complete orbits before the spacecraft lost sufficient power to remain operational in 2009.

Figure 2(top) shows the trajectory (distance and heliolatitude) of the Ulysses spacecraft throughout the lifetime of the mission. The fast-latitude scans can be readily identified by the time intervals when the spacecraft is closest to the Sun and the latitude changes rapidly from $-80°$ to $+80°$. The first of these passages occurs during solar minimum in 1994–95. There are additional fast-latitude scans during 2001 and 2007. The 2001 scan occurs at solar maximum, while the 2007 scan occurs during the rising activity phase toward solar maximum.

We compute the power spectra of all three components (R, T, N) in the same heliocentric coordinate system employed by Parker (1963) to describe the winding of the interplanetary

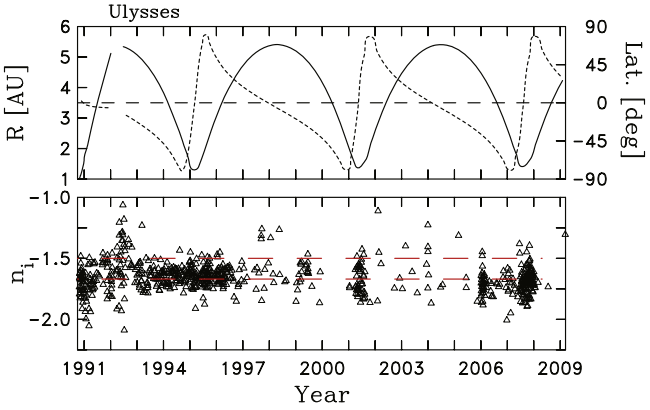

Figure 2. Trajectory of Ulysses spacecraft and power-law index of the measured power spectrum inertial range. The fast-latitude scans can be readily identified by the time intervals when the spacecraft is closet to the Sun and when the latitude changes rapidly from $-80°$ to $+80°$.

magnetic field spiral. From the spectra of the three components, we compute the trace of the power spectral matrix to obtain the spectrum of the total power. The spectrum of the $|B|$ time series is also computed as a measure of the compressive component. We then fit the resolved inertial-range frequencies of all five elements of the power spectra with a power-law form, f_{sc}^{n}, where f_{sc} is the fluctuation frequency in the spacecraft frame. In most instances, this means that we fit the frequency interval $2 < f_{sc} < 50$ mHz and excludes the frequency interval $0.8f_{p,c} < f_{sc} < 2.2f_{p,c}$, where $f_{p,c}$ is the proton cyclotron frequency, in order to avoid both enhanced power and polarization signatures associated with suprathermal H^{+}. In 18 instances a better fit was obtained using the frequency interval $0.5 < f_{sc} < 100$ mHz and excluding the frequency range $0.9f_{p,c} < f_{sc} < 4f_{p,c}$. Excluding frequencies near $f_{p,c}$ in this manner when performing spectral fits is not strictly necessary as we have chosen data intervals that do not show evidence of waves due to suprathermal protons. However, we are not certain that subtle effects are not introduced when these frequencies are included and excluding these frequencies does not impact the validity of our results. We do note that in some of the analyses shown here we focus on spacecraft-frame frequencies near the cyclotron frequency of relevant ions in order to examine polarization properties.

Figure 2(bottom) shows the fit power-law indices for the trace of the power spectral density matrix that were obtained as described above. There are 728 data intervals used in the making of this plot. There are relatively few results during the years 1997 through 2000, and 2002 through 2005. This occurs for several reasons and is partly due to the fact that our spectrogram code used to search both times of waves due to interstellar pickup ions (Marchuk et al. 2021) and these intervals of turbulence observations struggle when the measurement cadence changes. These years represent times when Ulysses was at the greatest heliocentric distances and the measurement cadence changed often. We made do with relatively short event intervals when studying the wave spectra, but this turbulence investigation greatly benefits from longer data intervals. For this reason, we struggled to obtain useful results during these years.

Our focus here is on the years 1993 through 1996, which begins 11 months after the Jovian flyby and ends 15 months before apoapsis (from 5.06 to 1.34 au and back to 4.67 au, and from $-23°$ southern latitude back to 19°.9 northern latitude).

This subset consists of 280 data intervals. Although not perfect, the appealing aspect of this subset is that the fit index is well described as lying in the range $-5/3 < n_i < -3/2$. This is the range of values normally expected for inertial-range spectra (Kolmogorov 1941; Iroshnikov 1964; Kraichnan 1965; Matthaeus & Zhou 1989).

Figure 3 shows the average plasma parameters for the years 1993–96 averaged over the duration of the time intervals used here. Parameters B and Θ_{BR} are averages computed directly from the 1 sec data. Parameters V_{SW}, N_P, and T_P are computed from the hourly averages of the Solar Wind Plasma Experiment (SWOOPS) data, while $\beta_P = 8\pi N_P k_B T_P/B^2$, the Alfvén speed $V_A = B(4\pi\rho)^{-1/2}$, and the Alfvén Mach number $M_A = V_{SW}/V_A$ are computed from the above means. As a matter of convenience, we can compute $\beta_P = 3.47 \times 10^{-5} N_P T_P/B^2$ and $V_A = 21.8BN_P^{1/2}$ using the variables in the units presented here.

Quasi-radial magnetic fields with $\Theta_{BR} < 30°$ are almost nonexistent in this ensemble. Since the orbit of Ulysses travels from the ecliptic plane at ~5 au to high southern latitudes at ~2 au then quickly to high northern latitudes at ~2 au, and then back to the ecliptic latitudes at ~5 au, the observed variation with time seen in most measurements is a combination of the dependence upon heliodistance and heliolatitude. The low-latitude observations during the fast scan are most evident in the plot of V_{SW}, where the wind speed is briefly reduced to <400 km s^{-1} in early 1995. Otherwise, $V_{SW} > 600$ km s^{-1}, except for the earliest and latest observations. This suggests that all but a relatively few intervals can be described as high-latitude solar-minimum observations. V_A is nearly constant throughout 1993–96 and climbs to higher values in 1994–95. With the exception of the fast-latitude scan, this represents times when the spacecraft was above 45° northern and southern latitude.

Figure 4 shows averages of the polarization spectra over the range $f_{p,c} < f_{sc} < 2f_{p,c}$ in the left column and $f_{He,c} < f_{sc} < 2f_{He,c}$, where $f_{He,c}$ is the cyclotron frequency of He^+ ions in the right columns. These are the frequency ranges where we expect to find elevated levels of D_{pol} and C_{oh}, with $|E_{lip}| \to 1$ signifying the presence of waves excited by newborn interstellar pickup ions or possibly other suprathermal ion populations. Note that $D_{pol} < 0.5$ in most cases and $C_{oh} < 0.5$ in all cases, while $|E_{lip}| < 0.25$ in all but a very few instances. The angle between the minimum-variance direction and the mean magnetic field, Θ_{kb}, can be any value. There is a tendency for lower values of Θ_{kB} near the start of 1995 when Ulysses performed a fast-latitude scan and was at its lowest latitude and closest to the Sun.

4. Magnetic Fluctuation Anisotropy

To analyze the measured anisotropy of the magnetic fluctuations, we define the following mean-field coordinate system: $\hat{\boldsymbol{Z}} = \boldsymbol{B}_0/|\boldsymbol{B}_0|$ is in the mean magnetic field direction, $\hat{\boldsymbol{Y}} = -\hat{\boldsymbol{Z}} \times \hat{\boldsymbol{R}}/|\hat{\boldsymbol{Z}} \times \hat{\boldsymbol{R}}|$ is perpendicular to both the radial direction and the mean-field direction, and $\hat{\boldsymbol{X}} = \hat{\boldsymbol{Y}} \times \hat{\boldsymbol{Z}}$ is perpendicular to both the $\hat{\boldsymbol{Y}}$ direction and the mean magnetic field direction $\hat{\boldsymbol{Z}}$. This means that $\hat{\boldsymbol{X}}$ has a nonzero projection onto the radial direction except for the singular instance where $\boldsymbol{B_0}$ is perpendicular to the radial direction. These are the same coordinates used by Belcher & Davis (1971) that established the transverse nature of magnetic fluctuations in the solar wind

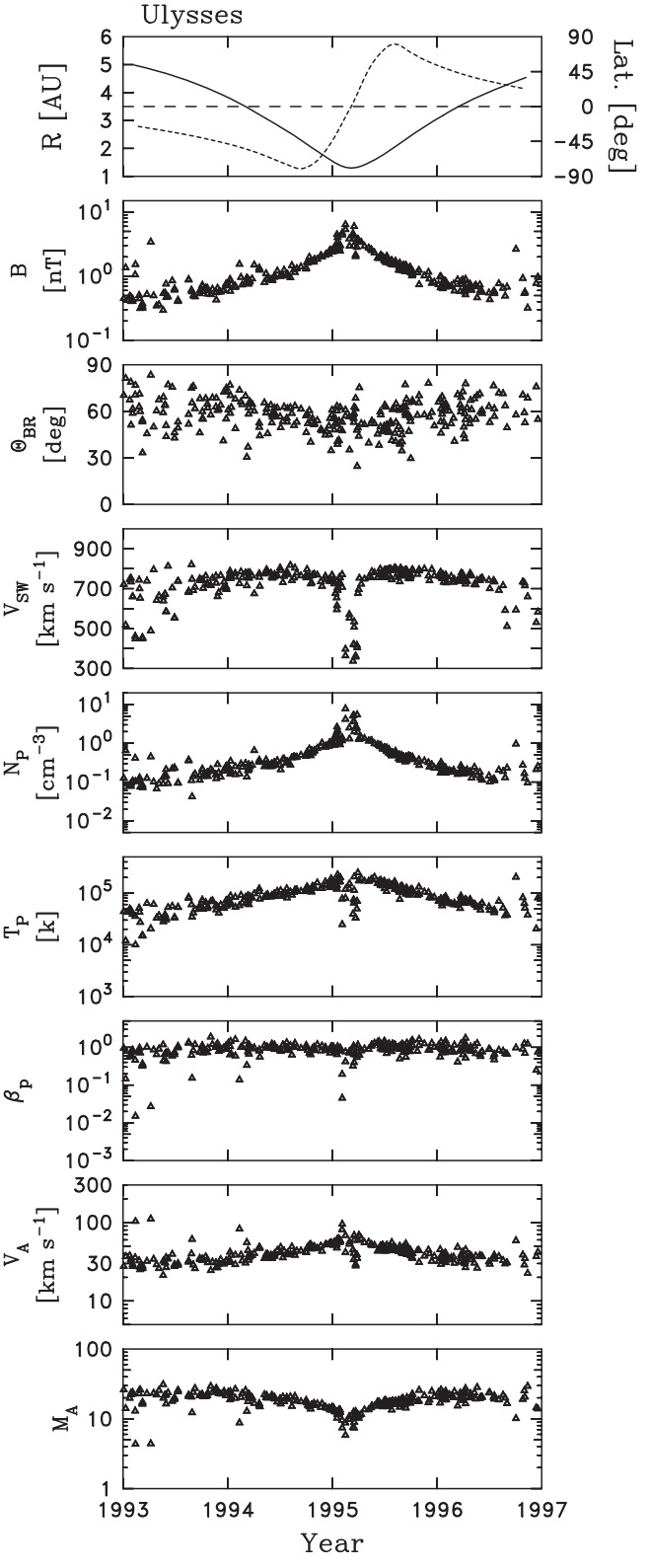

Figure 3. Ambient plasma parameters as measured by the Ulysses spacecraft from 1993 through 1996. Top to bottom: we plot the trajectory heliodistance and heliolatitude, the average magnetic field intensity, B, in nT, the angle between the mean field and the radial direction, Θ_{BR}, in degrees, the mean solar-wind speed, V_{SW}, in units of km s^{-1}, the thermal proton density, N_P, in units of cm^{-3}, the thermal proton density ,T_P, in units of Kelvin, the proton energy density parameter, β_P, the Alfvén speed, V_A, in units of km s^{-1}, and the Alfvén Mach number, M_A.

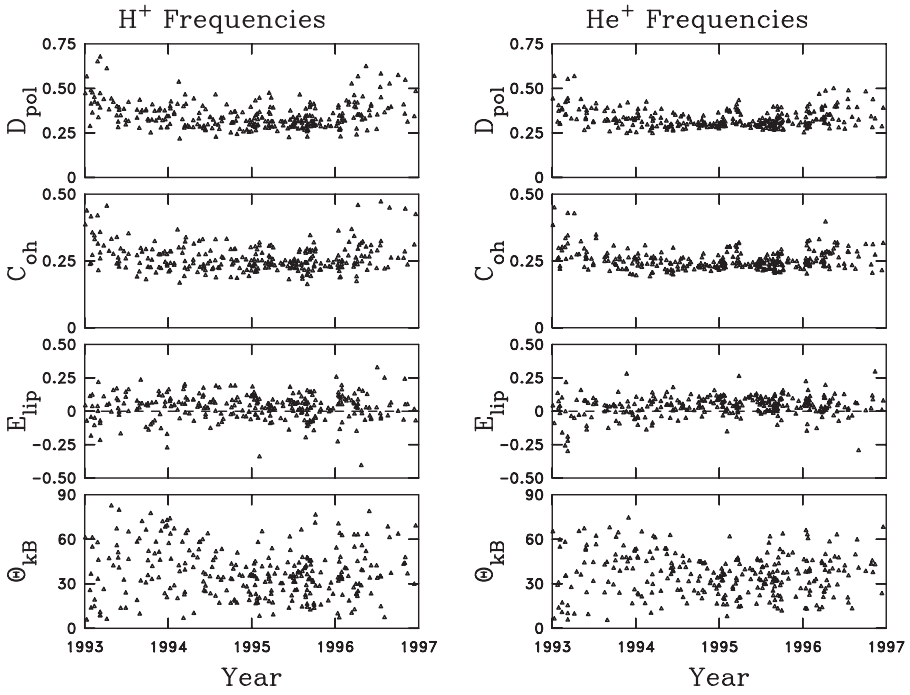

Figure 4. Polarization parameters averaged over the frequency range $f_{p,c} < f_{sc} < 2f_{p,c}$ (left) and $f_{He,c} < f_{sc} < 2f_{He,c}$ (right). Top to bottom: degree of polarization, D_{pol}, coherence, C_{oh}, ellipticity, E_{lip}, and angle between the minumum-variance direction and the mean magnetic field Θ_{kB}.

and was interpreted as evidence for the dominance of Alfvén waves propagating parallel to the mean magnetic field. When rotating to these mean-field coordinates, we compute the mean magnetic field, $\boldsymbol{B_0}$, to be the average of the magnetic field over the time interval used to compute the spectrum.

The fluctuation anisotropy is defined as the ratio of power associated with the perpendicular and parallel magnetic fluctuation $(P_{XX} + P_{YY})/P_{ZZ}$. Belcher & Davis (1971) found that in the data interval reported by them the ratio of P_{XX}: P_{YY}: $P_{ZZ} = 4:5:1$, which leads to $(P_{XX} + P_{YY})/P_{ZZ} = 9$. The central feature of their conclusions was that the energy of the parallel component of the magnetic fluctuation, P_{ZZ}, was only 10% of the total power, which implies that the magnetic fluctuations are largely transverse to the mean field and to a high degree noncompressive. No significance was assigned to $P_{XX} \neq P_{YY}$.

Smith et al. (2006c) demonstrated that the anisotropy of inertial-range fluctuations at 1 au possess a strong correlation upon both β_P and $\delta B/B_0$, where δB is the rms fluctuation level of the fluctuations. This apparent dual dependence arises from there being a strong correlation between the two variables. We repeat that analysis here using the Ulysses inertial-range spectra.

Figure 5 shows a plot of the above variance anisotropy as a function of β_P for each of the intervals used in this study. The line is reproduced from the analysis of ACE and Voyager data (Smith et al. 2006c; Pine et al. 2020c). High-latitude solar-minimum observations possess a high degree of uniformity, which explains why the range of β_P values is limited. While this limited range is responsible for a less-than-desirable independent fit to the data, reproduction of the fit from the 1 au analysis indicates a consistent result between the Ulysses and ACE observations.

Figure 6(a) shows our further analysis of the variance anisotropy based on ideas from nonlinear wave theory (Vasquez & Hollweg 2004) and compressible turbulence

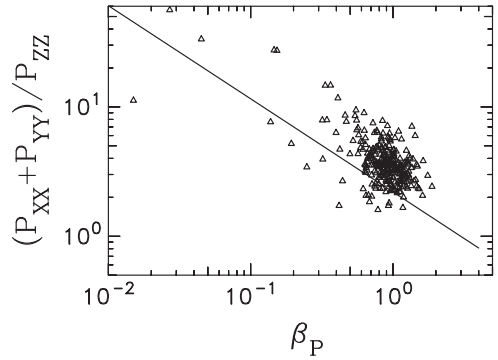

Figure 5. Dependence of variance anisotropy upon the proton pressure parameter β_P. The line is the same as was used to fit both open and closed field-line observations by the ACE spacecraft (Smith et al. 2006c).

theory (Matthaeus et al. 1996a) as previously shown in both ACE and Voyager data (Smith et al. 2006c; Pine et al. 2020c). It shows that the magnetic fluctuation anisotropy scales with the amplitude of the magnetic fluctuation when normalized by the mean magnetic field, suggesting that nonlinear processes may be important in the establishment of the fluctuation anisotropy. Unlike the earlier analyses, the range of values is more limited, but the correlation is still demonstrated. The underlying difficulty in separating this result from what is shown in Figure 5 is illustrated in panel (b), where the underlying correlation between β_P and $\delta B/B_0$ is demonstrated. Breaking this correlation down further, we can compare $N_P T_P$ versus δB in panel (c), where we see a strong correlation that could point to the role of turbulent heating of the plasma. Panel (d) maintains this correlation in a weakened form. However, panel (e) compares the fluctuation anisotropy directly with the computed rate of energy transport through the inertial range to heat the background plasma. Here we see an even weaker range of values and a less significant correlation. We believe the

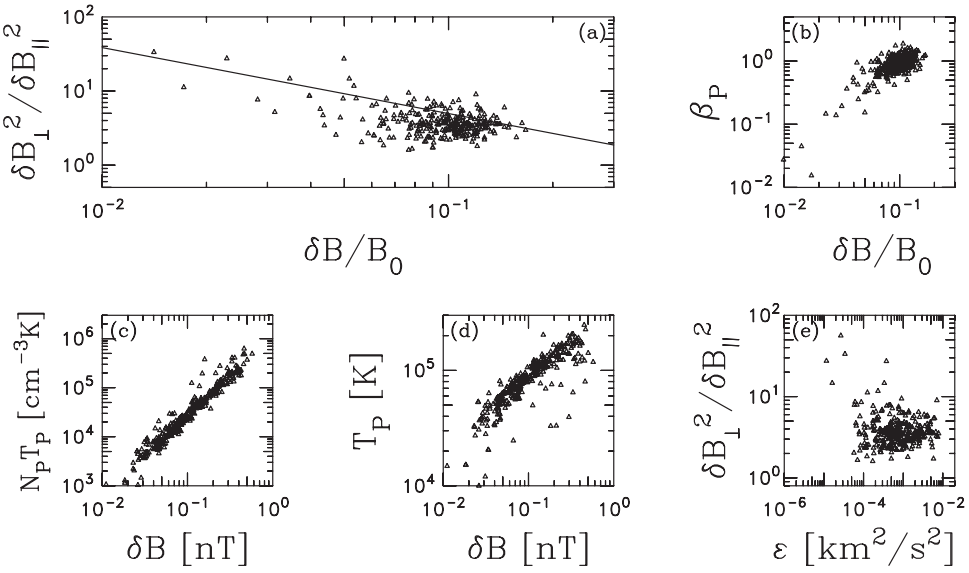

Figure 6. Further analysis of variance anisotropy based, in part, on ideas from nearly incompressible turbulence theory. The fit in panel (a) is the same as was used in Smith et al. (2006c) and Pine et al. (2020c).

correlation shown in panel (b) reflects either of two fundamental dynamics: either the strength of the turbulence as measured by the amplitude of the fluctuation spectrum or the strength of the mean field is determined at the solar source and the anisotropy is not the result of in situ dynamics, or the higher fluctuation level reflects stronger turbulence that leads to an elevated β_P. Panels (c) and (d) would seem to suggest that the correlation in panel (b) is not the result of a weakened mean-field intensity at the source and that in situ dynamics may explain what we see with elevated power levels leading to elevated temperatures. However, panel (e) clearly shows that the anisotropy is not related to the rate of energy transport through the spectrum.

5. Wavevector Anisotropy

Direct measurement of the underlying wavevector distribution is not possible using a single spacecraft. However, Batchelor (1953) has shown that even in isotropic hydrodynamic turbulence where there is no preferred direction, the spectrum of velocity fluctuations parallel to the separation vector (which is the radial direction in this analysis) will possess a different spectral amplitude to the perpendicular components. Bieber et al. (1996) have shown that a similar calculation can reveal the relative percent of energy distributed between wavevectors parallel and perpendicular to the mean magnetic field. That calculation uses the power spectra P_{XX} and P_{YY} and assumes that both have the same power-law index. Note that the $\hat{\boldsymbol{X}}$ direction has a nonzero projection onto the radial direction, which means it has a nonzero projection along the direction of the Fourier decomposition. This is critical to the analysis. It can then be shown that

$$\frac{P_{YY}}{P_{XX}} = \frac{k_S^{1-|n_i|} + r'\left(\frac{2\,|\,n_i\,|}{1+|\,n_i\,|}\right)k_2^{1-|n_i|}}{k_S^{1-|n_i|} + r'\left(\frac{2}{1+|\,n_i\,|}\right)k_2^{1-|n_i|}}, \tag{1}$$

where

$$k_2 = \frac{2\pi f_{\rm sc}}{V_{\rm SW}\sin\Theta_{\rm BR}} \tag{2}$$

is the 2D wavevector with projection at spacecraft-frame frequency $f_{\rm sc}$, and

$$k_S = \frac{2\pi f_{\rm sc}}{V_{\rm SW}\cos\Theta_{\rm BR}} \tag{3}$$

is the field-aligned wavevector with the same projection. $\Theta_{\rm BR}$ is the angle between the mean field and the radial direction that we define to be $0^\circ \leqslant \Theta_{\rm BR} \leqslant 90^\circ$, and $r' = C_2/C_S$ is the ratio of energy associated with the 2D and field-aligned components. The variation of P_{YY}/P_{XX} with $\Theta_{\rm BR}$ determines the ratio C_S/C_2, but regardless of that ratio $P_{YY}/P_{XX} = 1$ $(=|n_i|)$ at $\Theta_{\rm BR} = 0^\circ$ $(=90^\circ)$. This anisotropy is a result of the measurement and is not representative of the relative intensity of the magnetic fluctuation spectra P_{XX} and P_{YY} in the plasma frame, which is assumed to be equal (Bieber et al. 1996). However, it does represent the underlying anisotropy of the wavevectors in the parallel and perpendicular directions. It is also consistent with a simplified interpretation of the Maltese cross (Matthaeus et al. 1990). Equation (1) with varying $\Theta_{\rm BR}$ can be fit to obtain the underlying anisotropy of the wavevector relative to the mean field using a single spacecraft and has been used as a measure of the relative amount of 1D (field-aligned) and 2D geometries (Bieber et al. 1996; Leamon et al. 1998a; Hamilton et al. 2008; MacBride et al. 2010). It can also be used to explain the result of Belcher & Davis (1971), where $P_{YY}/P_{XX} \simeq 1.25$, indicating an 80:20 distribution of 2D and 1D wavevectors.

Each data interval is analyzed by computing the average and standard deviation of P_{YY}/P_{XX} over the range of frequencies fit. From the ratio of the component power spectra and the measured values of $\Theta_{\rm BR}$ and n_i, Equation (1) is used to compute r' and from that the fraction of total energy associated with the field-aligned wavevectors $R_{\rm SLAB} = C_S/(C_S + C_2)$. The weighted average and uncertainty of $R_{\rm SLAB}$ are then computed

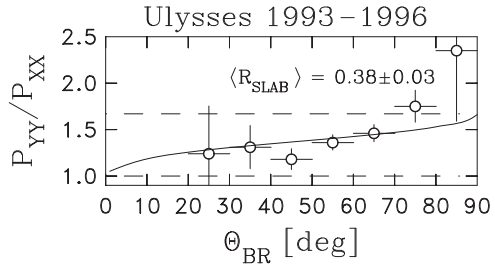

Figure 7. Weighted average and uncertainty of P_{YY}/P_{XX} binned by Θ_{BR}. There are no data intervals with $\Theta_{BR} < 20°$ and too few in the bin $80° < \Theta_{BR} < 90°$ to be useful. This results in a high uncertainty and essentially unusable weighted average in this bin.

using

$$\langle R_{SLAB} \rangle = \frac{\sum_i (r_i/\sigma_i)}{\sum_i (1/\sigma_i)}, \quad (4)$$

$$\langle \sigma_i \rangle = \left[\sum_i (1/\sigma_i) \right]^{-1/2}, \quad (5)$$

where r_i (σ_i) is the average (standard deviation) of P_{YY}/P_{XX} computed for each data interval i. For this analysis, we obtain $\langle R_{SLAB} \rangle = 0.38 \pm 0.03$.

A further test of this analysis is to see whether $\langle R_{SLAB} \rangle$ fit the expected variation with Θ_{BR}. The ensemble of magnetic spectra is divided according to Θ_{BR} into 10° bins with the weighted average of R_{SLAB} and σ computed for each bin and plotted in Figure 7. Rather than fit the results, we adopt the above average $\langle R_{SLAB} \rangle = 0.38$ and plot the expected functional form. With the exception of the highest bin, where there are only two examples, the expected functional form is a good fit to the distribution. We conclude that $\langle R_{SLAB} \rangle = 0.38 \pm 0.03$ provides a good description to the ensemble of observations resulting in 38% (62%) of the energy residing in field-aligned (perpendicular) wavevectors. The observations are dominated by the 2D component.

We should note that Hamilton et al. (2008) studied 960 data samples (567 open-field-line observations, 234 slow-wind observations with $V_{SW} < 400$ km s^{-1}, 219 intermediate-wind observations with $400 < V_{SW} < 500$ km s^{-1}, 101 fast-wind observations with $V_{SW} > 500$ km s^{-1}, and 13 intervals with no usable thermal ion data, and 393 magnetic cloud observations) using 1 au observations by the ACE spacecraft spanning the years 1998–2002. These are years surrounding solar maximum. They found that open field lines averaged 32% field-aligned wavevectors (50% for fast winds and 22% for slow winds) while magnetic clouds averaged 73% field-aligned wavevectors. We find here that the division of energy between parallel and perpendicular wavevectors during the high-latitude solar-minimum observations from 1 to 5 au by Ulysses are consistent with open-field-line observations at 1 au during solar maximum.

6. Turbulent Heating and Energy Transport

The fluctuation anisotropy analysis shown in Figures 5 and 6 has demonstrated that magnetic fluctuations are largely transverse to the local mean magnetic field. Despite the variability and the presence of smaller field-aligned components, which can be understood to reflect the presence of a compressive component, this anisotropy has often been interpreted as evidence that the magnetic fluctuations are comprised of parallel-propagating waves with field-aligned wavevectors. However, this same anisotropy is also consistent with 2D turbulence, where both magnetic fluctuations and wavevectors are confined to the 2D plane. Under the assumption that the spectrum is a composite of field-aligned and 2D wavevectors, the wavevector anisotropy analysis shown in Figure 7 resolves the average fraction of magnetic energy that is associated with the 2D component, which is 62% of the total fluctuation energy.

One of the fundamental underlying properties of fluid turbulence is that the nonlinear processes remake the energy of the fluctuations so as to move energy from large to small scales until some form of dissipation converts the coherent fluid-like fluctuations into heat. The spectral index that is fit from the inertial-range frequencies of the trace power spectra, as shown in Figure 2, is consistent with MHD extensions of hydrodynamic turbulence theory (Kolmogorov 1941; Matthaeus & Zhou 1989; Leamon et al. 1999; Smith 2009; Matthaeus & Velli 2011). This theory has been argued to be especially applicable to the incompressible 2D component where wave frequencies go to zero.

There are multiple complementary methods for obtaining estimates of the energy transport through the spectrum, often called the energy cascade, and the resulting thermal plasma heating. Vasquez et al. (2007) have shown that the average heating rate at 1 au scales as the product of the wind speed and thermal proton temperature, $V_{SW}T_P$. Extending this to heliodistances other than 1 au results in (Pine et al. 2020d)

$$\epsilon_V \equiv (5.3 \times 10^{-5}) V_{SW} T_P / R_{AU}, \quad (6)$$

where V_{SW} is given in units of km s^{-1}, T_P is temperature in units of K, and R_{AU} is heliocentric distance measured in units of au. Equation (6) yields the heating rate in units of J × kg $^{-1}$ × s^{-1}. Division by 10^6 yields units of km ^{2} × s^{-3} shown below. Note that this is derived as an average heating rate and not a prediction for individual data samples. The difficulty in applying this expression to the analysis here is that it assumes a single initial temperature at the source. This is not a reliable assumption when latitudinal variation is included in the database.

The second method is to employ the prediction that the fluctuation total energy spectrum varies as an extension of hydrodynamic theory (Matthaeus & Zhou 1989; Leamon et al. 1999; Smith 2009; Matthaeus & Velli 2011):

$$E_T(k) = C_K \epsilon_K^{2/3} k^{-5/3}, \quad (7)$$

where $E_T(k)$ is the omnidirectional spectrum of the total fluctuation energy and k is the wavevector. Simple arithmetic and application of the formalism to ACE and Voyager data to determine the unknown coefficient C_K (Vasquez et al. 2007; Pine et al. 2020d), and validation through application to analyses of wave excitation by suprathermal particles (Cannon et al. 2014b; Aggarwal et al. 2016; Fisher et al. 2016; Smith et al. 2017; Hollick et al. 2018b; Marchuk et al. 2021), yields

$$\epsilon_K = \frac{f_{sc}^{5/2} [E_M(f_{sc})]^{3/2} \cdot 21.8^3}{V_{SW} N_P^{3/2}}, \quad (8)$$

where $E_M(f_{sc})$ is the total measured magnetic field power spectral density in units of nT^2 Hz^{-1}, which is assumed to vary as $f_{sc}^{-5/3}$. N_P and 21.8^3 are part of the conversion of the

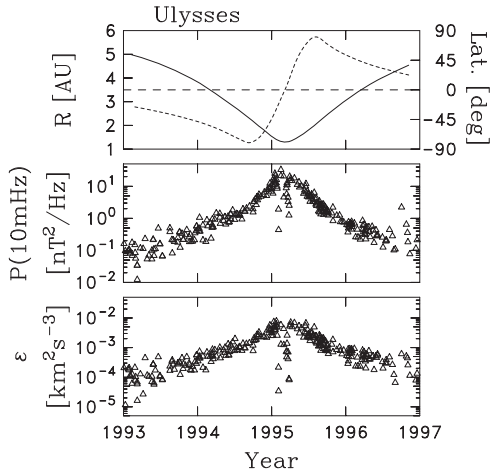

Figure 8. Top to bottom: the heliocentric distance and heliolatitude reproduced from Figure 2 of the Ulysses spacecraft from 1993 through 1996 during the first fast-latitude scan. Measured power spectrum level at 10 mHz for each data interval studied. Computed energy spectral transport rate (the plasma heating rate).

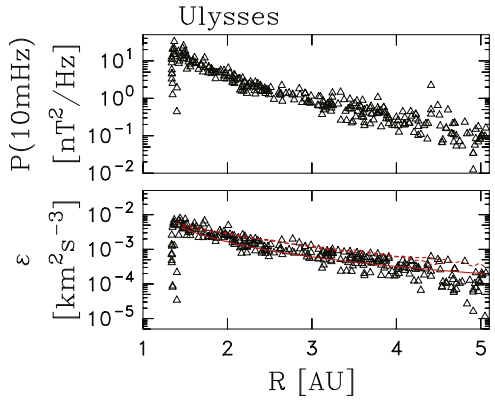

Figure 9. Top: measured power spectrum level at 10 mHz for each data interval studied, plotted as a function of heliocentric distance. Bottom: energy spectral transport rate, assumed to be the heating rate, computed at 10 mHz for each data interval studied using Equation (8). Solid red curve is obtained from the transport Equations (9)–(11). Twin dashed lines are obtained from Equation (6).

magnetic field to Alfvén units. We assume equipartition of kinetic and magnetic energy so that the Alfvén ratio $R_A = 1$. By this expression, ϵ_K is given in units of km^2 s^{-3}.

It is true that the observation of elevated correlation between the velocity and magnetic field fluctuations at high latitudes during solar minimum may mean that Equation (8) overestimates the turbulent energy cascade. This is the nature of so-called "imbalanced turbulence" or turbulence with high cross-helicity. However, Smith et al. (1995) examined the cross-correlation between the velocity and magnetic field fluctuations seen in the Ulysses data during the years we study here and found that the correlation varies from 0 to 0.8. This means a relative balance of Elsässer variables (Elsässer 1950) from 50:50 to 90:10. We can apply the scaling of third-moment theory as used by Zhou et al. (2004) to argue that the turbulent energy transport of the 90:10 imbalance is one-third the value of the balanced turbulence with the same power spectrum. Therefore, Equation (8) may overestimate the local heating rate by a factor of 3, but Smith et al. (1995) also showed that many data intervals during this same time show much lower levels of correlation.

The third method for obtaining the local spectral transport rate of the energy is obtained from third-moment theory (MacBride et al. 2005, 2008; Sorriso-Valvo et al. 2007; Marino et al. 2008; Carbone et al. 2009; Smith 2009; Stawarz et al. 2009, 2010, 2011; Wan et al. 2009; Forman et al. 2010; Osman et al. 2011; Coburn et al. 2012, 2014, 2015; Banerjee et al. 2016; Hadid et al. 2017; Smith et al. 2018; Sorriso-Valvo et al. 2018; Vasquez et al. 2018; Smith & Vasquez 2021). This is beyond the scope of this paper and requires accessing the highest-time-resolution thermal proton data.

Figure 8 shows our analysis of the turbulent heating rate using Equation (8). We choose the spacecraft-frame frequency 10 mHz because it lies consistently within the inertial range of the spectra. Figure 8 (top) shows the trajectory for reference. Figure 8 (middle) shows the computed power spectrum amplitude at 10 mHz derived from fits as demonstrated in Figure 1. The spectral level drops near closest approach and becomes more broadly distributed at the beginning and end of the time span. At all three times the spacecraft is at low latitudes. Otherwise, the results are a smoothly varying function of heliodistance. Figure 8(bottom) shows the computed energy cascade rate and corresponding heating rate as derived from Equation (8) and the measured magnetic power at 10 mHz. As with the computed power, the heating rate falls at closest approach and becomes more scattered at the greatest heliocentric distance, but is otherwise smoothly varying with heliodistance.

Figure 9 further illuminates the variation of the power spectral amplitude and ϵ_K with heliodistance. Figure 9 (top) plots the magnetic power at 10 mHz as a function of heliodistance. Figure 9 (bottom) plots the spectral cascade rate and equivalent turbulent heating rate. Black triangles represent the cascade and heating rates as computed from the magnetic spectra using Equation (8). Both halves of the trajectory shown overlapping in Figure 8, both inbound and outbound to closest approach and both south and north of the solar equator, overlay cleanly in both panels of Figure 9. There is no distinguishing difference between northern and southern hemispheres in either the power or turbulence levels. There is slightly greater scatter in the power level beyond 3 au when Ulysses is between $-65°$ southern and $+55°$ northern latitudes. These seem to be rather high latitudes to define as a streamer-belt source, and the wind speeds are consistently >700 km s^{-1}. The greater scatter becomes more significant beyond ~4.2 au, where Ulysses is inside $-40°$ southern and $+30°$ northern latitudes. The wind speed is still >700 km s^{-1} at these distances and the spacecraft is likely still observing a polar hole source.

Transport theory, as derived from the bulk parameters and large-scale fluctuations of the energy-containing range of hydrodynamics (Taylor 1935; von Kármán & Howarth 1938; Hossain et al. 1995; Biskamp 2003), can be applied to this data using extensions derived for MHD (Dobrowolny et al. 1980; Grappin et al. 1982; Hossain et al. 1995). It is the large-scale fluctuations that drive the turbulence, and these scales are not represented in these figures. However, transport theory based on these scales can be used to compare against the computed turbulence rates (Zhou & Matthaeus 1990a, 1990b; Matthaeus et al. 1994, 1996b, 1999a, 1999b; Williams & Zank 1994; Richardson et al. 1995, 1996; Williams et al. 1995; Zank et al. 1996; Smith et al. 2001; Isenberg et al. 2003; Richardson & Smith 2003; Breech et al. 2005, 2008, 2009, 2010; Isenberg 2005; Oughton et al. 2006, 2011; Smith et al. 2006c; Isenberg et al. 2010; Ng et al. 2010; Usmanov et al. 2012, 2014, 2014, 2018;

Zank et al. 2012; Adhikari et al. 2015a, 2015b, 2017; Zank et al. 2017) by computing the boundary conditions for the large-scale fluctuation energy using the hourly merged Ulysses data. MHD transport theory can be written in the following form (Smith et al. 2001, 2006b). The evolution of the total energy (magnetic plus kinetic) in the large-scale energy-containing fluctuations evolve radially in the steady-state solution according to

$$\frac{dZ^2}{dR} = -\frac{Z^2}{R} + \frac{C_{\rm sh} - M\sigma_D}{R}Z^2 + \frac{\dot{E}_{PI}}{V_{\rm SW}} - \frac{\alpha}{\lambda V_{\rm SW}}Z^3. \quad (9)$$

The similarity scale, which is most normally associated with the correlation scale, evolves according to

$$\frac{d\lambda}{dR} = \frac{M\sigma_D - \hat{C}_{\rm sh}}{R}\lambda - \frac{\beta}{\alpha}\lambda\frac{\dot{E}_{\rm PI}}{V_{\rm SW}Z^2} + \frac{\beta}{V_{\rm SW}}Z. \quad (10)$$

The thermal proton temperature evolves according to

$$\frac{dT_P}{dR} = -\frac{4}{3}\frac{T_P}{R} + \frac{1}{3}\frac{m_p}{k_B}\frac{\alpha}{V_{\rm SW}}\frac{Z^3}{\lambda}. \quad (11)$$

The parameters in Equations (9)–(11) are typical of those used previously (Zhou & Matthaeus 1989; Zank et al. 1996; Matthaeus et al. 1996b, 1999b, 2004; Smith et al. 2001) and identical to those used by Smith et al. (2006b) and Pine et al. (2020d) that successfully reproduced the low-latitude observations of Voyager 2. Choosing the von Kármán–Taylor constants $\alpha/\beta = 2$ preserves the turbulent viscosity. As before, we use here $\alpha = 0.8$, $\beta = 0.4$. We select the mixing constant $M = 1/3$ and the normalized energy difference parameter $\sigma_D = -1/3$. We use the shear terms $C_{\rm sh} = 1.4$ and $\hat{C}_{\rm sh} = 0$, which represents an R^{-1} scaling of energy injection via shear with no additional effect on the similarity scale.

While these choices accurately reproduce the low-latitude observations over both solar-minimum and solar-maximum conditions, these choices may or may not be appropriate to higher latitude observations and we use them here only as an example. We compute Z^2 from the merged (MAG + SWOOPS) hourly Ulysses data is used to compute 10 hr means and variances, and the resulting variance of the total energy is taken to be Z^2. From this we take the boundary conditions at 1.35 au to be $Z^2 = 650$ km^2 s^{-2}, $V_{\rm SW} = 750$ km s^{-1}, $N_P = 1.5$ cm^{-3}, $V_A = 60$ km s^{-1}, $T_P = 2.5 \times 10^5$ K, and $\lambda = 0.016$ au. The value for the similarity scale is half what is used for low-latitude transport analyses. Turbulence driving via wave-energy excitation by newborn interstellar pickup ions is treated in the same manner as before (Smith et al. 2006c; Pine et al. 2020d) using the analysis of pickup-ion wave excitation described by Marchuk et al. (2021).

The solid red curve in Figure 9 (bottom) shows the result of this transport analysis. Although we are forced to assume a single set of parameters for the inner boundary due to the absence of additional measurements at high latitudes, the theory fits the observations remarkably well. The observations diverge from the theory at the smallest and largest heliocentric distances because Ulysses is at the lowest latitudes at these points and the boundary conditions for low-latitude turbulence differ from those used here to characterize the high latitudes. The two dashed red curves in Figure 9 (bottom) use 27 day averages of the measured wind speed and proton temperature to compute the energy cascade and heating rate using Equation (6). The solar inbound and outbound halves of the orbit are shown separately, but are indistinguishable until ~4 au. This again demonstrates the strong repeatability in the Ulysses data at high latitudes during solar minimum as well as the overall agreement between the three different techniques for computing the thermal proton heating.

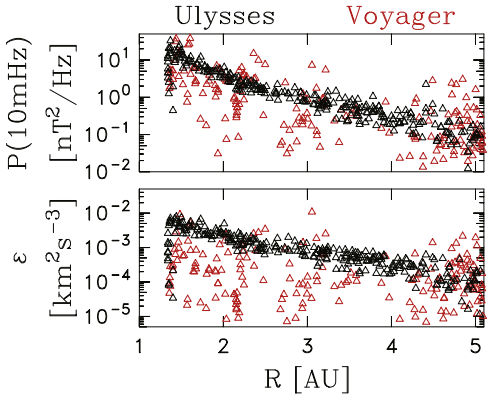

Figure 10. Top to bottom: measured power spectrum level and computed energy spectral transport rate at 10 mHz for Ulysses (black) and Voyager (red) plotted as a function of heliocentric distance, R.

This lends further evidence to support the claim that high-latitude solar-minimum observations are turbulent and dynamic in very much the same manner as the lower-latitude observations during solar maximum. The greater uniformity of the flow and the published imbalance of the turbulence would be expected to provide a significantly weaker turbulence level. However, the elevated levels of turbulence seen by the Ulysses spacecraft at this time greatly exceeds the factor of 3 that the cross-correlation can explain.

To emphasize this point, we show Figure 10, where the Voyager observations from 1977–79 that were analyzed by Pine et al. (2020a, 2020b, 2020c, 2020d, 2020e) are shown in red. The important aspect of the comparison is that both the magnetic power spectrum levels and the associated turbulent cascade and heating rates are lower at Voyager than at Ulysses. Since Voyager traversed the range 1–5 au at lower latitudes than Ulysses and during the approach to solar maximum, it is especially noteworthy that turbulence levels seen by Ulysses are notably higher than those seen by Voyager. Equality between the two results is not seen until ~4.2 au, when Ulysses reaches lower latitudes, but is still within the high-speed wind. Even here, there is less scatter in the observations by Ulysses than are seen by Voyager, and this is almost certainly attributable to the established uniformity of solar-wind conditions in the Ulysses measurements at these latitudes at this phase of the solar cycle.

Last, we compare the turbulence rate to the rate of wave excitation by newborn interstellar pickup ions. Marchuk et al. (2021) has examined the question of wave generation and continues to argue that waves can only be seen when excitation exceeds the rate at which turbulence remakes the fluctuations. There are no observed waves due to pickup ions in any of the spectra used here. However, the absence of observable waves does not mean that wave excitation is not an active dynamic. In fact, the absence of waves means that the turbulence has absorbed that energy and contributed it to the energy cascade that heats the background. This raises the question: to what degree does wave excitation by interstellar ions contribute to plasma heating in these observations? Figure 11 compares the computed energy cascade and associated plasma heating as

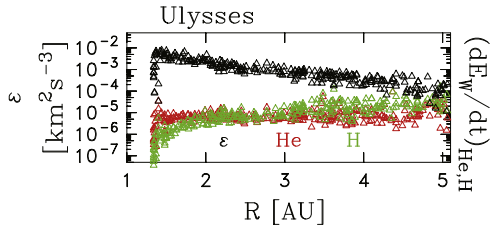

Figure 11. Comparison of spectral transport rate, ϵ, against the rate of wave-energy excitation by newborn interstellar pickup He^+ (red) and H^+ (green).

derived from Equation (8) and validated by transport theory in Figure 9 against the rate of wave-energy excitation by newborn interstellar pickup He^+ (red) and H^+ (green). As Ulysses approaches 5 au the contributions approach, but do not achieve, equality. Interstellar pickup ions do not become the dominant turbulence-driving term until 10 au (Pine et al. 2020d). Throughout this analysis, the large-scale fluctuations in the solar wind remain the dominant source of energy that drives the observed turbulence.

7. Summary

We have examined Ulysses magnetic field data from 1993 through 1996, during solar minimum as the spacecraft passed from $-80°$ southern latitude to $+80°$ northern latitude. We used daily spectrograms to identify and exclude data intervals that contain waves attributable to suprathermal particles, including waves due to newborn interstellar ions and shocks, thereby creating a database of turbulence observations. While some intervals were found to have these waves, they were mainly gathered toward the beginning and end of the observed timeline. This allowed us to use a majority of the spectrograms within this timeline, resulting in a 280 element database of turbulent observations primarily from high latitudes during solar minimum. Due to the highly elliptical orbit of Ulysses—which traveled between ∼5 au and ∼2 au while spanning both high and low latitudes—the observed variation found in most measurements is a combination of the dependence upon heliodistance and heliolatitude. Due to the fast-latitude scan near periapsis, relatively few intervals used here can be described as low-latitude solar-minimum observations. There are some additional observations near the beginning and end of the time interval studied that exhibit low-latitude solar-wind parameters.

Each interval in the study was used to compute the variance anisotropy, that is, the ratio of magnetic energy in the components perpendicular and parallel to the mean magnetic field. The high-latitude solar-minimum characteristics of these intervals were shown to depend on β_P in the very same manner as has been seen in the low-latitude ACE and Voyager observations. Further analysis of the variance anisotropy based on nonlinear wave theory and compressible turbulence theory shows that the magnetic fluctuation anisotropy scales with the amplitude of the magnetic fluctuation when normalized by the mean magnetic field, as has been seen at low latitudes. This suggests that nonlinear processes may be important in the establishment of the fluctuation anisotropy.

Using the computed magnetic power spectra at 10 mHz in the spacecraft, we were able to analyze the magnetic power as a function of heliodistance and helioaltitude. The spectral level drops near closest approach, and becomes more broadly distributed at the beginning and end of the time span. At all three times, the spacecraft is at low latitudes. Otherwise, the results are a smoothly varying function of heliodistance. Still using the 10 mHz power level, we were able to analyze the energy cascade rate, which we assume to be equal to the thermal plasma heating rate. The heating rate, which is computed from a combination of the magnetic power level, wind speed, and density, falls at closest approach and becomes more scattered at the greatest heliocentric distance, consistent with the observed power levels, but otherwise smoothly varies with heliodistance. It is also found that the cascade rate tends to have greater scatter in the power level beyond 3 au, when Ulysses is between $-65°$ southern and $+55°$ northern latitudes. These seem to be rather high latitudes to define a streamer-belt source, and the wind speeds are consistently >700 km s^{-1}. The greater scatter becomes more significant beyond ∼4.2 au, where Ulysses is inside $-40°$ southern and $+30°$ northern latitudes.

Transport theory was used to compare computed turbulence rates, resulting in further evidence supporting the claim that high-latitude solar-minimum observations are at least as equally turbulent and dynamic as the low-latitude observations during solar maximum. Perhaps due to the lack of solar activity, and despite the established high degree of correlation between the magnetic and velocity fluctuations, the high-latitude solar-minimum conditions show a stronger level of turbulence and greater rates of energy cascade through the spectrum than is seen at low latitudes during this same time. To further support this point, we compare our findings to Voyager observations from 1977–79, where both the magnetic power spectrum levels, their associated turbulent cascade, and the heating rates are lower at Voyager then at Ulysses. Traditionally, the high degree of correlation between the magnetic and velocity fluctuations, consistent with wave propagation away from the Sun, has been taken as one indication that the high-latitude turbulence is less evolved than at lower latitudes. The greater turbulence levels shown here may support that interpretation. The unknown consideration is whether the turbulence is created at similar levels close to the Sun. Lastly, comparing turbulence rates to the wave excitation by newborn interstellar pickup ions, as analyzed by Marchuk et al. (2021), leads to the conclusion that wave excitation by interstellar ions does not contribute significantly to plasma heating in these observations.

C.W.S., P.A.I., S.H., and Z.B.P. are supported by NASA grant No. NNX17AB86G. C.W.S., B.J.V., P.A.I., A.S.W., and A.V.M. are supported by NASA HSR grant No. 80NSSC18K1215. C.W.S., B.J.V., P.A.I., and N.A.S. were partially supported by NASA grant No. 80NSSC17K0009. B.J.V. is supported by NASA grant No. 80NSSC19K0832. C.J. J. and N.A.S. are supported by the Interstellar Boundary Explorer mission as a part of NASAs Explorer Program, partially by NASA SR&T grant No. NNG06GD55G, and the Sun-2-Ice (NSF grant No. AGS1135432) project. M.B. and M. A.K. acknowledge support by the Polish National Science Center grant No. 2015/19/B/ST9/01328. The data used in this analysis are available from the National Space Science Data Center.

Appendix
Time Interval Listings

Table 1 lists the time intervals used in this study.

Table 1
Ulysses Observations of Turbulence Time Intervals

Year	Time [DOY::Hour:Min]	Time [DOY::Hour:Min]	Time [DOY::Hour:Min]	Time [DOY::Hour:Min]
1993	003/02:00-14:01	010/00:00-07:00	024/00:00-12:00	028/00:01-09:01
	028/16:01-21:01	034/00:00-12:00	034/00:00-14:01	043/04:01-12:00
	044/03:01-11:01	057/00:00-02:00	058/11:01-14:01	060/16:01-23:02
	068/18:01-20:01	068/09:01-16:01	068/04:01-16:01	084/02:00-07:01
	097/04:01-16:01	107/00:00-12:00	117/12:00-21:01	126/00:00-06:01
	140/04:01-19:00	141/02:00-12:00	147/00:00-11:01	147/00:00-12:00
	150/12:00-23:02	151/02:00-12:00	157/12:00-18:01	172/00:00-12:00
	180/00:00-12:00	180/02:00-12:00	192/02:00-16:01	192/04:01-16:01
	229/07:00-18:01	229/02:00-16:01	239/04:01-18:02	241/07:00-14:01
	245/07:00-19:00	251/04:01-16:01	268/00:00-12:00	269/07:00-10:00
	277/02:00-11:00	277/00:00-12:00	280/00:00-09:00	289/00:00-12:00
	294/07:00-16:01	296/02:00-15:01	306/09:01-16:01	312/02:00-19:00
	324/04:01-14:01	326/03:00-06:00	330/00:00-12:00	334/00:00-13:01
	341/00:00-12:00	350/00:00-12:00	353/01:00-08:00	360/02:00-16:01
	361/00:02-10:00	361/02:00-12:00		
1994	003/00:01-06:01	008/12:01-20:01	009/12:00-20:01	010/12:00-19:00
	013/00:00-12:00	027/00:00-09:01	027/11:00-19:00	041/10:02-19:01
	047/07:00-09:01	051/03:00-07:01	062/12:00-21:01	067/08:00-17:00
	071/09:01-16:01	073/00:00-12:00	074/00:00-07:00	078/00:00-12:00
	085/12:00-23:02	074/15:01-23:02	093/00:00-12:00	110/10:02-16:01
	110/12:00-21:01	112/10:02-23:01	128/09:01-23:02	134/13:00-23:01
	136/17:01-22:01	139/12:00-23:02	151/12:01-18:00	154/12:00-21:01
	154/12:00-23:02	157/11:00-15:02	163/12:00-19:00	163/12:00-23:01
	164/01:00-9:014	173/16:01-23:02	183/09:01-19:01	185/09:01-19:00
	193/00:00-07:00	197/09:01-19:01	206/12:00-19:00	207/09:01-19:00
	209/07:00-14:01	219/07:00-19:00	224/12:00-18:00	232/00:00-07:00
	235/00:00-07:00	241/07:00-19:00	256/09:01-14:02	274/00:00-07:00
	274/00:00-21:01	277/00:00-19:00	280/00:00-16:01	285/00:00-14:01
	290/00:00-12:00	293/03:01-13:00	296/00:00-14:01	301/13:00-19:00
	303/00:00-13:00	313/00:00-12:00	325/10:02-19:00	329/12:00-21:01
	341/00:00-12:00	344/00:00-15:01	353/12:00-21:01	355/04:01-12:00
	357/01:00-12:00	361/06:01-10:01	364/12:01-17:00	364/12:00-21:01
1995	004/09:01-19:00	007/13:02-16:01	011/12:01-17:01	011/12:00-23:02
	015/12:00-20:01	016/12:00-19:00	017/00:00-04:01	018/12:00-19:00
	019/02:01-07:02	023/13:00-19:01	024/09:01-21:01	027/12:00-19:00
	028/09:01-19:00	034/12:00-20:01	035/00:00-06:00	046/16:01-18:01
	046/07:00-19:00	059/18:00-23:02	060/09:01-19:00	072/12:00-21:01
	074/15:01-22:01	075/09:01-19:00	076/09:01-19:00	077/00:01-03:02
	081/18:00-23:02	081/09:01-23:02	086/00:00-05:01	087/04:01-12:00
	089/15:01-22:00	092/18:00-23:02	094/19:00-23:02	101/02:00-19:00
	112/09:01-23:02	127/04:01-19:00	135/07:00-21:01	138/02:00-16:01
	147/07:00-21:01	158/09:01-19:00	163/19:01-22:01	167/10:02-22:01
	168/09:01-21:01	169/19:01-23:02	175/17:01-23:02	177/09:01-21:01
	181/16:00-23:02	182/04:01-19:00	183/13:00-23:02	187/12:00-23:02
	189/14:01-23:02	190/07:02-23:02	196/15:00-23:02	198/02:00-14:01
	203/19:00-23:00	203/12:00-23:02	207/14:01-23:02	210/17:01-23:02
	217/16:01-23:02	218/14:01-23:02	220/18:00-23:02	222/19:00-23:02
	222/02:00-14:01	231/14:01-23:02	234/13:01-23:02	235/17:00-23:02
	236/18:01-23:02	238/16:01-23:02	239/04:01-19:00	242/17:01-23:02
	243/00:00-12:00	243/04:01-10:02	243/13:00-20:01	244/00:00-04:01
	246/15:01-22:01	249/02:00-15:01	254/15:00-23:02	255/00:00-04:01
	256/16:01-23:02	257/00:00-04:01	259/04:01-14:01	260/16:01-23:02
	266/00:00-09:00	267/08:00-13:00	267/09:01-21:01	272/01:00-10:00
	273/01:00-12:00	274/02:00-07:00	278/04:01-14:01	280/03:00-06:00
	280/01:00-15:01	297/00:00-16:01	302/00:00-16:01	303/09:01-12:01
	321/09:01-21:01	336/00:02-03:01	339/00:00-16:01	347/00:00-16:01
	356/00:00-12:00			
1996	005/09:01-23:02	011/14:01-21:01	013/03:01-09:01	014/12:01-23:01
	015/02:00-08:00	018/18:01-20:01	018/14:01-23:02	020/21:01-23:02
	023/09:01-23:02	024/01:01-09:01	029/09:01-16:01	030/02:00-06:00

Table 1
(Continued)

Year	Time [DOY::Hour:Min]	Time [DOY::Hour:Min]	Time [DOY::Hour:Min]	Time [DOY::Hour:Min]
	030/00:00-23:02	031/02:02-11:00	032/09:01-23:02	043/09:01-23:02
	050/07:02-13:02	058/09:01-23:02	061/07:00-19:00	073/00:00-04:00
	081/09:01-23:02	084/04:01-14:01	085/03:01-09:01	085/19:00-23:02
	091/05:00-13:01	094/13:01-17:01	094/07:00-19:00	098/09:02-11:01
	098/04:01-14:01	100/05:01-09:01	100/19:00-23:02	105/15:01-23:02
	115/09:01-12:00	116/00:00-16:01	118/02:00-15:01	121/13:02-22:01
	131/03:01-12:00	136/05:00-07:00	141/00:01-03:00	150/07:00-13:02
	152/15:01-22:00	158/04:01-10:01	158/02:00-12:00	182/00:00-12:00
	185/00:00-12:00	198/09:01-18:01	201/03:02-07:02	201/00:00-09:01
	217/00:01-03:00	231/09:01-23:02	239/00:00-02:00	245/19:00-21:01
	276/16:01-18:02	300/00:00-16:01	306/04:01-07:00	308/04:01-07:00
	317/12:00-23:02	347/07:00-19:00	353/14:01-23:02	

ORCID iDs

Abigale S. Watson https://orcid.org/0000-0003-2057-5891
Charles W. Smith https://orcid.org/0000-0002-5379-1542
Anastasia V. Marchuk https://orcid.org/0000-0002-7408-5671
Matthew R. Argall https://orcid.org/0000-0001-6315-1613
Philip A. Isenberg https://orcid.org/0000-0003-0505-8546
Bernard J. Vasquez https://orcid.org/0000-0001-8593-7289
Nathan A. Schwadron https://orcid.org/0000-0002-3737-9283
Maciej Bzowski https://orcid.org/0000-0003-3957-2359
Marzena A. Kubiak https://orcid.org/0000-0002-5204-9645

References

Adhikari, L., Zank, G. P., Bruno, R., et al. 2015a, ApJ, 805, 63
Adhikari, L., Zank, G. P., Bruno, R., et al. 2015b, JPhCS, 642, 012001
Adhikari, L., Zank, G. P., Hunana, P., et al. 2017, ApJ, 841, 85
Aggarwal, P., Taylor, D. K., Smith, C. W., et al. 2016, ApJ, 822, 94
Argall, M. R., Fisher, M. F., Joyce, C. J., et al. 2015, GeoRL, 42, 9617
Argall, M. R., Hollick, S. J., Pine, Z. B., et al. 2017, ApJ, 849, 61
Argall, M. R., Hollick, S. J., Pine, Z. B., et al. 2018, ApJ, 854, 77
Banerjee, S., Hadid, L. Z., Sahraoui, F., & Galtier, S. 2016, ApJL, 829, L27
Batchelor, G. K. 1953, The Theory of Homogeneous Turbulence (New York: Cambridge Univ. Press)
Belcher, J. W., & Davis Jr., L. 1971, JGR, 76, 3534
Bieber, J. W., Wanner, W., & Matthaeus, W. H. 1996, JGR, 101, 2511
Biskamp, D. 2003, Magnetohydrodynamic Turbulence (New York: Cambridge Univ. Press)
Blackman, R. B., & Tukey, J. W. 1958, The Measurement of Power Spectra (Mineola, NY: Dover)
Breech, B., Cranmer, S. R., Matthaeus, W. H., Kasper, J. C., & Oughton, S. 2010, in AIP Conf. Proc. 1216, Twelfth International Solar Wind Conference (Melville, NY: AIP), 214
Breech, B., Matthaeus, W. H., Cranmer, S. R., Kasper, J. C., & Oughton, S. 2009, JGRA, 114, A09103
Breech, B., Matthaeus, W. H., Minnie, J., et al. 2005, GeoRL, 32, L06103
Breech, B., Matthaeus, W. H., Minnie, J., et al. 2008, JGRA, 113, A08105
Cannon, B. E., Smith, C. W., Isenberg, P. A., et al. 2013, in AIP Conf. Proc. 1539, Solar Wind 13 (Melville, NY: AIP), 334
Cannon, B. E., Smith, C. W., Isenberg, P. A., et al. 2014a, ApJ, 784, 150
Cannon, B. E., Smith, C. W., Isenberg, P. A., et al. 2014b, ApJ, 787, 133
Cannon, B. E., Smith, C. W., Isenberg, P. A., et al. 2017, ApJ, 840, 13
Carbone, V., Marino, R., Sorriso-Valvo, L., Noullez, A., & Bruno, R. 2009, PhRvL, 103, 061102
Chen, J. 1989, PhD Thesis, Univ. Delaware, Newark
Coburn, J. T., Forman, M. A., Smith, C. W., Vasquez, B. J., & Stawarz, J. E. 2015, RSPTA, 373, 20140150
Coburn, J. T., Smith, C. W., Vasquez, B. J., Forman, M. A., & Stawarz, J. E. 2014, ApJ, 786, 52
Coburn, J. T., Smith, C. W., Vasquez, B. J., Stawarz, J. E., & Forman, M. A. 2012, ApJ, 754, 93
Dobrowolny, M., Mangeney, A., & Veltri, P. 1980, A&A, 83, 26
Elsässer, W. M. 1950, PhRv, 79, 183
Fisher, M. K., Argall, M. R., Joyce, C. J., et al. 2016, ApJ, 830, 47
Forman, M. A., Smith, C. W., & Vasquez, B. J. 2010, PhRvL, 104, 189001
Fowler, R. A., Kotick, B. J., & Elliott, R. D. 1967, JGR, 72, 2871
Grappin, R., Frisch, U., Léorat, J., & Pouquet, A. 1982, A&A, 105, 6
Hadid, L. Z., Sahraoui, F., & Galtier, S. 2017, ApJ, 838, 9
Hamilton, K., Smith, C. W., Vasquez, B. J., & Leamon, R. J. 2008, JGR, 113, A01106
Hollick, S. J., Smith, C. W., Pine, Z. B., et al. 2018a, ApJ, 863, 75
Hollick, S. J., Smith, C. W., Pine, Z. B., et al. 2018b, ApJ, 863, 76
Hollick, S. J., Smith, C. W., Pine, Z. B., et al. 2018c, ApJS, 237, 34
Hossain, M., Gray, P. C., Pontius Jr., D. H., Matthaeus, W. H., & Oughton, S. 1995, PhFl, 7, 2886
Howes, G. G., Cowley, S. C., Dorlund, W., et al. 2008a, JGRA, 113, A05103
Howes, G. G., Dorland, W., Cowley, S. C., et al. 2008b, PhRvL, 100, 065004
Howes, G. G., Dorland, W., Cowley, S. C., et al. 2008c, PhRvL, 101, 149502
Iroshnikov, P. S. 1964, SvA, 7, 566
Isenberg, P. A. 2005, ApJ, 623, 502
Isenberg, P. A., Smith, C. W., & Matthaeus, W. H. 2003, ApJ, 592, 564
Isenberg, P. A., Smith, C. W., Matthaeus, W. H., & Richardson, J. D. 2010, ApJ, 719, 716
Joyce, C. J., Smith, C. W., Isenberg, P. A., Murphy, N., & Schwadron, N. A. 2010, ApJ, 724, 1256
Kolmogorov, A. N. 1941, DoSSR, 30, 301, (Reprinted in Proc. R. Soc. London A, 434, 9-13, 1991)
Kraichnan, R. H. 1965, PhFl, 8, 1385
Leamon, R. J., Smith, C. W., & Ness, N. F. 1998b, GeoRL, 25, 2505
Leamon, R. J., Smith, C. W., Ness, N. F., Matthaeus, W. H., & Wong, H. K. 1998a, JGR, 103, 4775
Leamon, R. J., Smith, C. W., Ness, N. F., & Wong, H. K. 1999, JGR, 104, 22331
MacBride, B. T., Forman, M. A., & Smith, C. W. 2005, in Proc. Solar Wind 11: Connecting Sun and Heliosphere. ESA SP-592, ed. B. Fleck & T. H. Zurbuchen (The Netherlands: European Space Agency), 613
MacBride, B. T., Smith, C. W., & Forman, M. A. 2008, ApJ, 679, 1644
MacBride, B. T., Smith, C. W., & Vasquez, B. J. 2010, JGRA, 115, A07105
Marchuk, A. V., Smith, C. W., Watson, A. S., et al. 2021, ApJ, 923, 185
Marino, R., Sorriso-Valvo, L., Carbone, V., et al. 2008, ApJ, 677, L71
Markovskii, S. A., Vasquez, B. J., & Smith, C. W. 2008, ApJ, 675, 1576
Markovskii, S. A., Vasquez, B. J., & Smith, C. W. 2015, ApJ, 806, 78
Matthaeus, W. H., Ghosh, S., Oughton, S., & Roberts, D. A. 1996a, JGR, 101, 7619
Matthaeus, W. H., & Goldstein, M. L. 1982, JGR, 87, 6011
Matthaeus, W. H., Goldstein, M. L., & Roberts, D. A. 1990, JGR, 95, 20673
Matthaeus, W. H., Minnie, J., Breech, B., et al. 2004, GeoRL, 31, L12803
Matthaeus, W. H., Oughton, S., Pontius Jr., D. H., & Zhou, Y. 1994, JGR, 99, 19267
Matthaeus, W. H., Smith, C. W., & Bieber, J. W. 1999b, in AIP Conf. Proc. 471, Solar Wind 9, ed. S. R. Habbal et al. (Melville, NY: AIP), 511
Matthaeus, W. H., & Velli, M. 2011, SSRv, 160, 145
Matthaeus, W. H., Zank, G. P., & Oughton, S. 1996b, JPlPh, 56, 659

Matthaeus, W. H., Zank, G. P., Smith, C. W., & Oughton, S. 1999a, PhRvL, 82, 3444
Matthaeus, W. H., & Zhou, Y. 1989, PhFlB, 1, 1929
Means, J. D. 1972, JGR, 77, 5551
Mish, W. H., Wenger, R. M., Behannon, K. W., & Byrnes, J. B. 1982, Interactive Digital Signal Processor, NASA Technical Memorandum 83997 (Greenbelt, MD: Goddard Space Flight Center), https://ntrs.nasa.gov/citations/19840026903 (Revised 1984)
Ng, C. S., Bhattacharjee, A., Munsi, D., Isenberg, P. A., & Smith, C. W. 2010, JGRA, 115, A02101
Osman, K. T., Wan, M., Matthaeus, W. H., Weygand, J. M., & Dasso, S. 2011, PhRvL, 107, 165001
Oughton, S., Dmitruk, P., & Matthaeus, W. H. 2006, PhPl, 13, 042306
Oughton, S., Matthaeus, W. H., Smith, C. W., Breech, B., & Isenberg, P. A. 2011, JGRA, 116, A08105
Parker, E. N. 1963, Interplanetary Dynamical Processes (New York: Wiley-Interscience)
Pine, Z. B., Smith, C. W., Hollick, S. J., et al. 2020a, ApJ, 900, 91
Pine, Z. B., Smith, C. W., Hollick, S. J., et al. 2020b, ApJ, 900, 92
Pine, Z. B., Smith, C. W., Hollick, S. J., et al. 2020c, ApJ, 900, 93
Pine, Z. B., Smith, C. W., Hollick, S. J., et al. 2020d, ApJ, 900, 94
Pine, Z. B., Smith, C. W., Hollick, S. J., et al. 2020e, ApJS, 250, 14
Rankin, D., & Kurtz, R. 1970, JGR, 75, 5444
Richardson, J. D., Paularena, K. I., Lazarus, A. J., & Belcher, J. W. 1995, GeoRL, 22, 1469
Richardson, J. D., Phillips, J. L., Smith, C. W., & Gray, P. C. 1996, GeoRL, 23, 3259
Richardson, J. D., & Smith, C. W. 2003, GeoRL, 30, 1206
Smith, C. W. 2009, in Heliophysics I. Plasma Physics of the Local Cosmos, ed. C. J. Schrijver & G. Siscoe (Cambridge: Cambridge Univ. Press), 163
Smith, C. W., Aggarwal, P., Argall, M. R., et al. 2017, JPhCS, 900, 012018
Smith, C. W., Hamilton, K., Vasquez, B. J., & Leamon, R. J. 2006a, ApJL, 645, L85
Smith, C. W., Isenberg, P. A., Matthaeus, W. H., & Richardson, J. D. 2006b, ApJ, 638, 508
Smith, C. W., Matthaeus, W. H., & Ness, N. F. 1990, ICRC, 5, 280
Smith, C. W., Matthaeus, W. H., Zank, G. P., et al. 2001, JGR, 106, 8253
Smith, C. W., & Vasquez, B. J. 2021, FrASS, 7, 114
Smith, C. W., Vasquez, B. J., Coburn, J. T., Forman, M. A., & Stawarz, J. E. 2018, ApJ, 858, 21
Smith, C. W., Vasquez, B. J., & Hamilton, K. 2006c, JGRA, 111, A09111
Smith, C. W., Vasquez, B. J., & Hollweg, J. V. 2012, ApJ, 745, 8
Smith, E. J., Balogh, A., Neugebauer, M., & McComas, D. 1995, GeoRL, 22, 3381
Sorriso-Valvo, L., Carbone, F., Perri, S., et al. 2018, SoPh, 293, 10
Sorriso-Valvo, L., Marino, R., Carbone, V., et al. 2007, PhRvL, 99, 115001
Stawarz, J. E., Smith, C. W., Vasquez, B. J., Forman, M. A., & MacBride, B. T. 2009, ApJ, 697, 1119
Stawarz, J. E., Smith, C. W., Vasquez, B. J., Forman, M. A., & MacBride, B. T. 2010, ApJ, 713, 920
Stawarz, J. E., Vasquez, B. J., Smith, C. W., Forman, M. A., & Klewicki, J. C. 2011, ApJ, 736, 44
Taylor, G. I. 1935, RSPSA, 151, 421
Usmanov, A. V., Goldstein, M. L., & Matthaeus, W. H. 2012, ApJ, 754, 40
Usmanov, A. V., Goldstein, M. L., & Matthaeus, W. H. 2014, ApJ, 788, 43
Usmanov, A. V., Goldstein, M. L., & Matthaeus, W. H. 2014, ApJ, 820, 17
Usmanov, A. V., Matthaeus, W. H., Goldstein, M. L., & Chhiber, R. 2018, ApJ, 865, 25
Vasquez, B. J., Forman, M. A., Coburn, J. T., Smith, C. W., & Stawarz, J. E. 2018, ApJ, 867, 156
Vasquez, B. J., & Hollweg, J. V. 2004, JGRA, 109, A05103
Vasquez, B. J., Smith, C. W., Hamilton, K., MacBride, B. T., & Leamon, R. J. 2007, JGRA, 112, A07101
von Kármán, T., & Howarth, L. 1938, RSPSA, 164, 192
Wan, M., Sevidio, S., Oughton, S., & Matthaeus, W. H. 2009, PhPl, 16, 090703
Williams, L. L., & Zank, G. P. 1994, JGR, 99, 19229
Williams, L. L., Zank, G. P., & Matthaeus, W. H. 1995, JGR, 100, 17059
Zank, G. P., Adhikari, L., Hunana, P., et al. 2017, ApJ, 835, 147
Zank, G. P., Dosch, A., Hunana, P., et al. 2012, ApJ, 745, 35
Zank, G. P., Matthaeus, W. H., & Smith, C. W. 1996, JGR, 101, 17093
Zhou, Y., & Matthaeus, W. H. 1989, GeoRL, 16, 755
Zhou, Y., & Matthaeus, W. H. 1990a, JGR, 95, 10291
Zhou, Y., & Matthaeus, W. H. 1990b, JGR, 95, 14881
Zhou, Y., Matthaeus, W. H., & Dmitruk, P. 2004, RvMP, 76, 1015